Deformation mechanisms for superplastic behaviors in a dual-phase high specific strength steel with ultrafine grains

Wei Wang[a,b], Muxin Yang[a], Dingshun Yan[a], Ping Jiang[a], Fuping Yuan[a,b,*], Xiaolei Wu[a,b]

[a] *State Key Laboratory of Nonlinear Mechanics, Institute of Mechanics, Chinese Academy of Science, No.15, North 4th Ring, West Road, Beijing 100190, People's Republic of China*
[b] *School of Engineering Science, University of Chinese Academy of Sciences, Beijing 100190, People's Republic of China*

ARTICLE INFO

ABSTRACT

The superplastic behaviors of a high specific strength steel (HSSS) with dual-phase microstructure and ultrafine grains have been investigated under a temperature range of 873–973 K and at a wide strain rate range of 10^{-4}–10^{-1}/s. The ultrafine grained HSSS exhibits excellent superplastic properties. The microstructure observations at interrupted strains for tests under temperature of 973 K and at strain rate of 10^{-3}/s have provided evidences of different mechanisms for two stages. At the first stage (strain range from 0% to 400%), the superplastic flow is attributed to the diffusional transformation from fcc austenite phase to intermetallic compound B2 phase coupled with grain boundary sliding. While intragranular dislocation activities should be the dominant mechanism for the second stage (strain range from 400% to 629%) due to the increased realistic strain rate by diffusive necking. The grain sizes of both phases are observed to be relatively stable and remain always submicron level during the high temperature tensile deformation, facilitating the superplastic flow.

1. Introduction

Metals and alloys generally break with relatively small elongations (< 100%) when subjected to uniaxial tensile loading at room temperature. High elongation to fracture, i.e., superplasticity is possible to be achieved under certain conditions [1–14]. It is now well established that two fundamental conditions should be satisfied in order to achieve superplastic deformation in metals and alloys: 1) High homologous temperature (generally with a testing homologous temperature of $T/T_m > 0.5$, where T_m is the absolute melting temperature) is needed; 2) A relative small grain size is required since grain boundary sliding (GBS) is an important deformation mechanism during superplastic flow and GB density increases with decreasing grain size. Previous studies have also indicated that ultrafine grained (UFG) metals processed by severe plastic deformation (SPD) can achieve excellent superplastic properties in bulk materials [15,16]. However, these two requirements are generally incompatible in pure metals and solid solution alloys due to the easy grain growth at high temperatures. Thus, the UFG metals are better to either consist of dual-phase or contain finely dispersed second phase, which can inhibit grain growth.

Stronger, tougher and lighter steels are always desirable in various industry or defense applications. Such expectations have been realized in recent decades by low-density steels, which are mainly based on Fe-Al-Mn-C alloy system and are so called TRIPLEX steels. These TRIPLEX steels generally consist of fcc austenite, bcc ferrite and finely dispersed nanometer-sized κ-carbides with (Fe, Mn)$_3$AlC type [17–23]. More recently, Kim et al. [24] has developed a high specific strength steel (HSSS) with composition of Fe-16Mn-10Al-0.86C-5Ni (weight %), which consists of both fcc austenite phase and intermetallic compound B2 phase. This HSSS shows excellent combination of specific strength and elongation when compared to the other low-density metals and alloys. In our previous research [25,26], it has been shown that this UFG HSSS should be better understood as a dual-phase microstructure since the B2 phase is deformable. Thus, the stress/strain partitioning between the constituent phases and the back-stress-induced strain hardening should play important roles during the plastic deformation for this HSSS.

Superplasticity is of both academic and industrial interests because it provides basis for producing complex parts [27]. Superplastic forming may be more widely used if the superplasticity can be achieved under lower deformation temperatures and at higher deformation strain rates [1,28,29]. The UFG HSSS (Fe-16Mn-10Al-0.86C-5Ni, weight %) has the potential for the application in automobile industry due to its excellent mechanical properties. This UFG HSSS also has potential for

easy superplastic forming in the industry due to its dual-phase microstructure and small grain size. However, the superplastic behaviors and the corresponding deformation mechanisms of this HSSS under high temperature tensile deformation are still unknown. In this regard, the UFG HSSS was produced first by cold rolling and subsequent short-time annealing. Then, the superplastic flow behaviors of this UFG HSSS were studied by tensile tests under a temperature range of 600–700 ℃ and at a wide strain rate range of 10^{-4}–10^{-1}/s, and the corresponding mechanisms for superplasticity are investigated by a series of interrupted tests at varying strains and the subsequent microstructure observations.

2. Materials and experimental procedures

The details for the preparation of the HSSS can be found in our previous papers [25,26]. The hot-rolled plates with a thickness of 7.3 mm were cold rolled into a final thickness of 1.5 mm, and then were annealed at 1173 K for 15 min followed immediately by water quenching. The tensile specimens for the superplastic tests have a gauge section of $10 \times 4 \times 1.5$ mm^3, and the tensile direction is parallel to the rolling direction. All surfaces of the specimens were carefully polished to remove any irregularities. High-temperature uniaxial tensile tests were performed on an MTS Landmark testing machine with temperatures from 873 to 973 K and engineering strain rates of 10^{-4}–10^{-1} s^{-1}. In order to ensure uniform temperature distributions, the specimens were held for 5 min at the given temperatures before tensile testing.

Followed by cold rolling and annealing, the microstructures of the HSSS were characterized by electron back-scattered diffraction (EBSD) and transmission electron microscopy (TEM). The details of the sample preparations and the operation procedures for obtaining EBSD and TEM images can be found in our previous papers [25]. The "frozen" microstructures from the interrupted tests (extracted from the center part of the gauge section) were also revealed by EBSD to investigate the deformation mechanisms of the superplastic flow in this HSSS. During the EBSD acquisition, a scanning area of $40 \times 40 \ \mu m^2$ was chosen and a scanning step of 0.07 μm was used. Grain boundaries (GBs) are defined by misorientations larger than 15°. Texture is calculated using rank 16 harmonic series expansion with 5 degree Gaussian smoothing. The favored slip system is deduced by sorting the Schimd factor of potential slip systems at each EBSD nodes. Kernel average misorientation (KAM) is calculated against all neighbors within 280 nm distance (the misorientation angles larger than 2° are excluded) [30].

3. Results and discussions

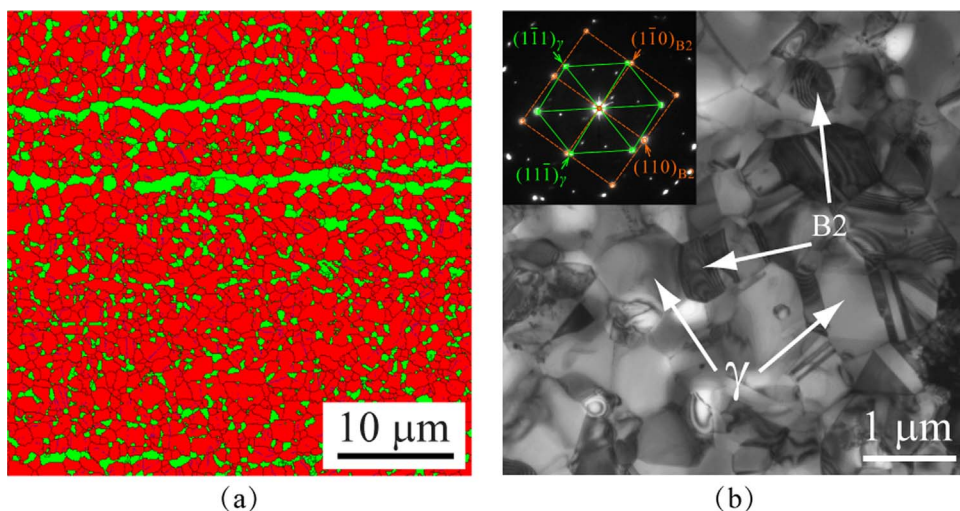The microstructures of the specimens prior to high-temperature tensile tests are shown in Fig. 1. In the EBSD phase image (Fig. 1(a)), two phases are clearly visible, in which one is the fcc γ-austenite phase with equiaxed grains and the other is the B2 phase (FeAl intermetallic compound) with both granular and lamellar grains. In the TEM image (Fig. 1(b)), the B2 phase is observed to be much inclined to precipitate at either GBs or triple junctions of γ-austenite matrix, instead of the γ grain interiors. Annealing twins are often seen in the γ-austenite grains. The corresponding indexed selected area diffraction patterns for both phases are also displayed in the inset of Fig. 1(b). The average grain size is about 0.934 μm for the fcc γ-austenite phase while is about 0.475 μm for the B2 phase prior to high-temperature tensile tests. The area fraction of γ-austenite is about 82% while the area of B2 phase is about 18% for the untested sample.

The engineering stress-strain curves under different elevated temperatures (873, 923, 973 K) for the HSSS are shown in Fig. 2(a), (b) and (c), respectively. After elastic deformation, the flow stress reaches the peak stress rapidly. With further tensile deformation, the flow stress decreases slowly, and stays at a steady state (with a very small stress level) for a long strain interval before the final fracture at low strain rates. However, the flow stress decreases directly to the final fracture rapidly at high strain rates. The undeformed and the final fracture shapes for the sample under temperature of 973 K and at strain rate of 10^{-3}/s are also shown in the inset of Fig. 2(c). Obviously, the flow behaviors are highly dependent on the deformation conditions. The flow softening rate after peak stress is observed to decrease monotonically with increasing temperature and decreasing strain rate.

Fig. 3(a) shows the elongation to fracture and the maximum flow stress as a function of strain rate. The logarithmic coordinates are used for the strain rate and the maximum flow stress. The peak flow stress is observed to increase monotonically with decreasing temperature and increasing strain rate. These trends could be due to the following aspects: 1) The lower deformation temperature might reduce the effects of dynamic softening due to the decreasing thermal activation process; 2) The higher strain rate might decelerate the dislocation annihilation thus increase the dislocation density. The elongation to fracture increases with increasing temperature. At lower temperatures (873, 923 K), the elongation to fracture decreases monotonically with increasing strain rate. However, the elongation to fracture increases first and then decreases with increasing strain rate at higher temperature (973 K). At the same strain rate (10^{-3}/s), the normalized deformation temperature (T/T_m, where T_m is the melting temperature) is plotted against the elongation to fracture in Fig. 3(b) for the HSSS, along with the data for the other steels and the intermetallic compounds [1,4,10,12,14]. As observed, the HSSS displays excellent superplastic properties when compared to the other steels and the intermetallic compounds. For example, when compared with the duplex stainless steel (DPSS) steel and the TiAl intermetallic compound, the normalized deformation temperature for

Fig. 1. (a) EBSD phase distribution for the untested sample. (b) TEM image for the untested sample. In (a), the red color is for the fcc austenite phase while the blue color is for the B2 phase. The same color coding is used for the following figures with phase distribution. The inset of (b) shows the indexed selected area diffraction pattern for the TEM image with an electron beam closely parallel to both the $[011]_\gamma$ and $[001]_{B2}$ zone axes. (For interpretation of the references to color in this figure legend, the reader is referred to the web version of this article).
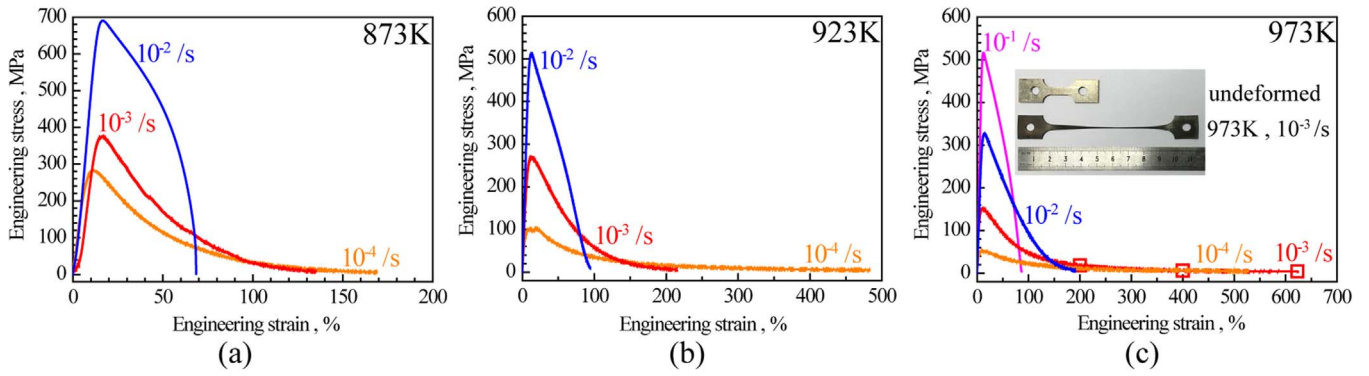
Fig. 2. The tensile properties of the HSSS at a wide range of strain rates and under different elevated temperatures: (a) 873 K; (b) 923 K; (c) 973 K. Several interrupted tests at varying strains (200%, 400%, 629%, marked as squares in the (c)) have been conducted under temperature of 973 K and at strain rate of 10^{-3}/s.

this HSSS is much lower when the elongations to fracture are similar (~ 200%). Moreover, when compared with the hyper-eutectoid steel (HES), the Martensitic steel and the FeAl intermetallic compound, the normalized deformation temperature for this HSSS is also lower when the elongations to fracture are similar (~ 600%). The HSSS shows the highest superplasticity (629%) under temperature of 973 K and at strain rate of 10^{-3}/s, thus several interrupted tests at varying strains (200%, 400%, 629%) have also been conducted in order to investigate the corresponding deformation mechanisms for the superplastic behaviors.

The EBSD phase distributions at varying times under static annealing (under temperature of 973 K and without deformation) are shown in Fig. 4(a-c). While, Fig. 4(d-f) show the EBSD phase distributions at varying times under high temperature tensile deformation (under temperature of 973 K and strain rate of 10^{-3}/s). It should be noted that the time intervals for EBSD images are exactly the same for both static annealing condition and high temperature tensile deformation condition. The evolutions for volume fraction of B2 phase as a function of time are shown in Fig. 4(g) for both conditions. It is observed that the B2 phase with lamellar shape has a tendency to turn into granular shape under high temperature tensile deformation, while the lamellar B2 precipitates are reserved under static annealing condition. Moreover, although the phase transformation from fcc austenite phase to B2 phase occurred during the static annealing, the transformation

was found to be enhanced during high temperature tensile deformation under the same temperature.

The phase transformation was observed to take place randomly, and the average grain size of the B2 phase is plotted as a function of time for both static annealing and high temperature tensile deformation in Fig. 5(a), which clearly follows the well-known $t^{1/2}$ diffusion rule. A classical equation can be used to calculate the flow activation energy in the HSSS as following:

$$\dot{\varepsilon} = A\sigma^{1/m} \exp(\frac{-Q}{RT}) \tag{1}$$

where $\dot{\varepsilon}$ is the strain rate, σ is the maximum flow stress, m is SRS, Q is the activation energy, T is the deformation temperature, A is a material constant. The logarithmic value of the maximum flow stress as a function of 10000/T is plotted in Fig. 5(b) for this HSSS. Thus, the activation energy during the superplastic flow behavior of this HSSS can be estimated as:

$$Q = \frac{R}{m} \frac{\partial \ln \sigma}{\partial (\frac{1}{T})} \tag{2}$$

Taking the average value for SRS (m) in the temperature range of 923–973 K for this HSSS, the activation energy Q can be estimated to be about 216 kJ/mol, which is very similar to the value for solute element diffusion in the literature [31]. Moreover, this value of Q for the HSSS is
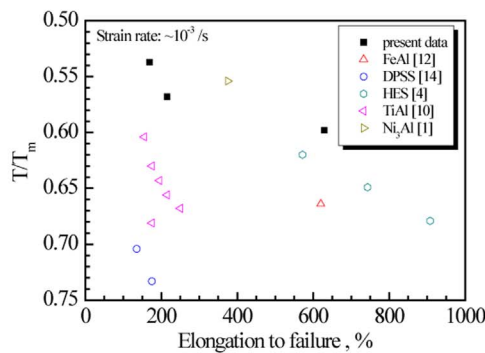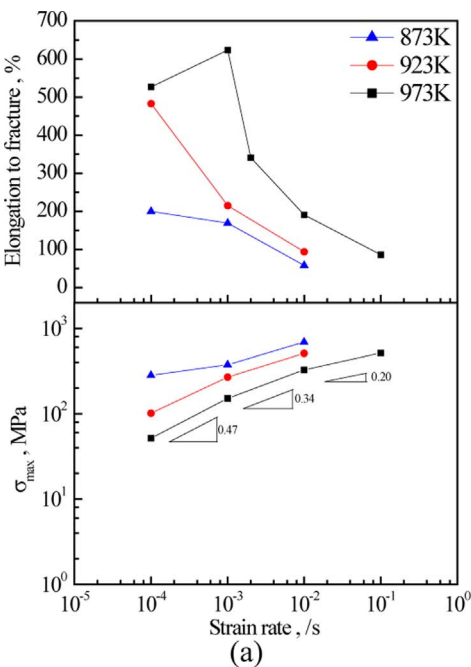

Fig. 3. (a) Variations of the elongation to fracture (upper) and the maximum flow stress (lower) as a function of the imposed strain rate for the HSSS tested under different elevated temperatures. (b) The normalized deformation temperature vs. the elongation to fracture for the HSSS, along with the data for the other steels and the intermetallic compounds [1,4,10,12,14]. In (a), the strain rate sensitivities (SRS, m) are also given for the experiments conducted at 973 K.
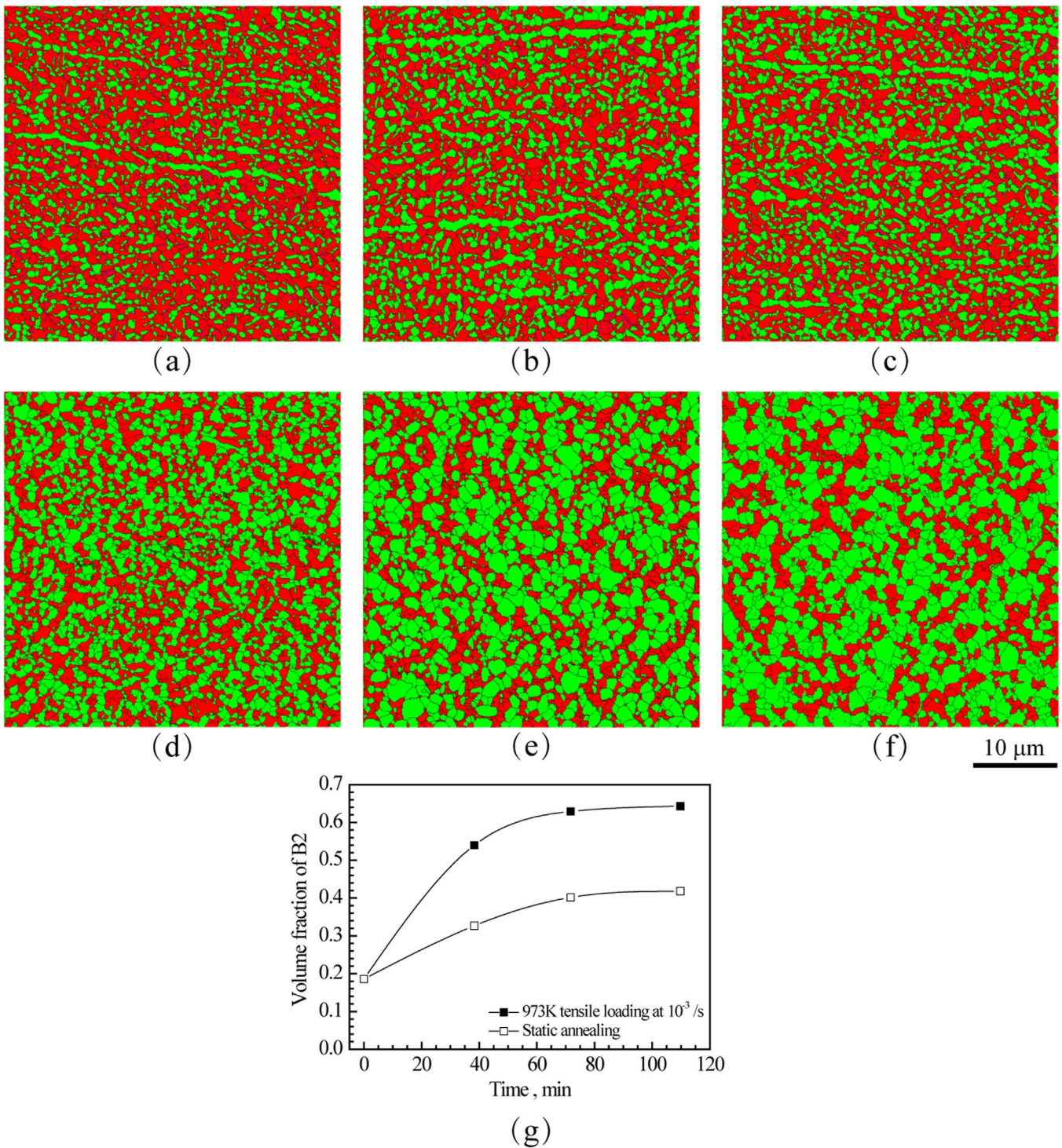
Fig. 4. The EBSD phase distributions under static annealing (under temperature of 973 K) at varying times: (a) 38 min; (b) 72 min; (c) 110 min. The EBSD phase distributions under high temperature tensile deformation (under temperature of 973 K and strain rate of 10^{-3}/s) at varying times: (d) 38 min; (e) 72 min; (f) 110 min (g) The evolutions of volume fraction of B2 phase as a function of time for both conditions.

much lower than the creep activation energy of 370 kJ/mol reported for binary Fe-28Al [32] and 450 kJ/mol reported for binary Fe-40Al [33]. The lower flow activation energy for this HSSS indicates that the superplastic deformation process in this HSSS should be controlled by subboundary and grain-boundary diffusion instead of by lattice diffusion [34].

As we know, the well-known Avrami equation can be used to describe how solids transform from one phase to another phase at constant temperature, the transformation characteristic exponent n is usually an indicator whether or not the transformation is diffusion controlled or diffusionless, and is also an indicator of what type of diffusion controlled growth [31,35]. The Avrami equation can be described as follows:

$$V'_{B_2} = 1 - \exp(-kt^n) \tag{3}$$

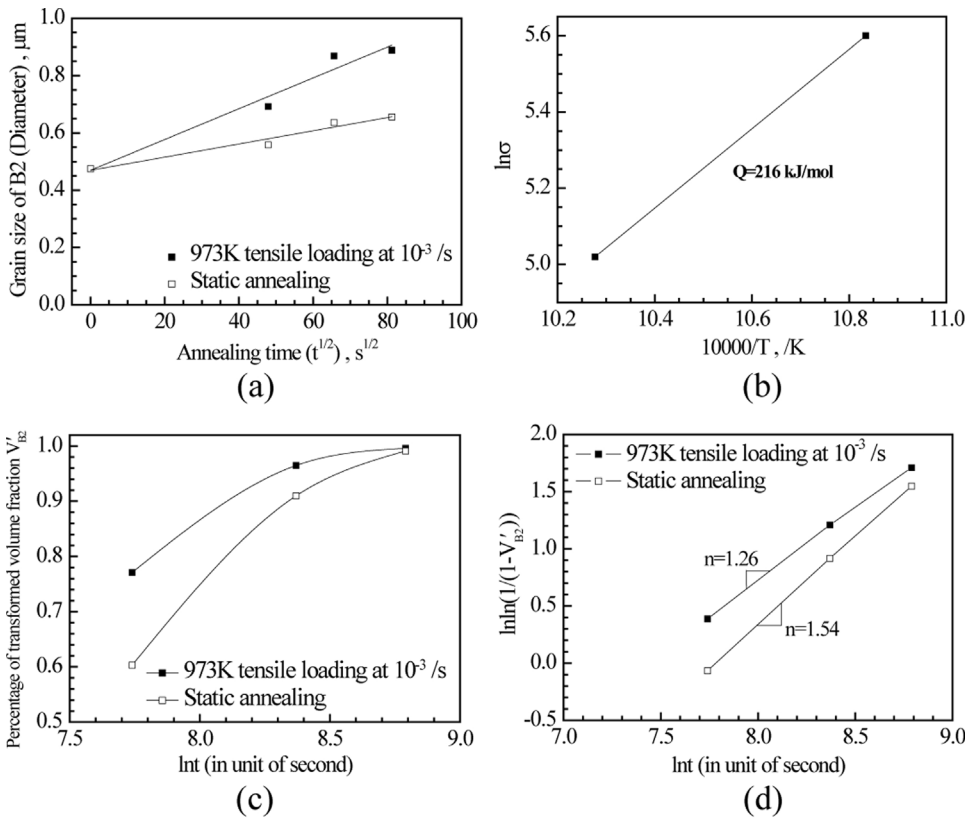$$\ln \ln\left(\frac{1}{1 - V'_{B_2}}\right) = k + n(\ln t) \tag{4}$$

Fig. 6. The EBSD IPF images under high temperature tensile deformation (under temperature of 973 K and strain rate of 10^{-3}/s) for fcc austenite phase: (a) $\varepsilon = 0$; (b) $\varepsilon = 200\%$; (c) $\varepsilon = 400\%$; (d) $\varepsilon = 629\%$. (e) The corresponding grain size distributions at varying tensile strains. (f) The corresponding misorientation angle distributions at varying tensile strains.
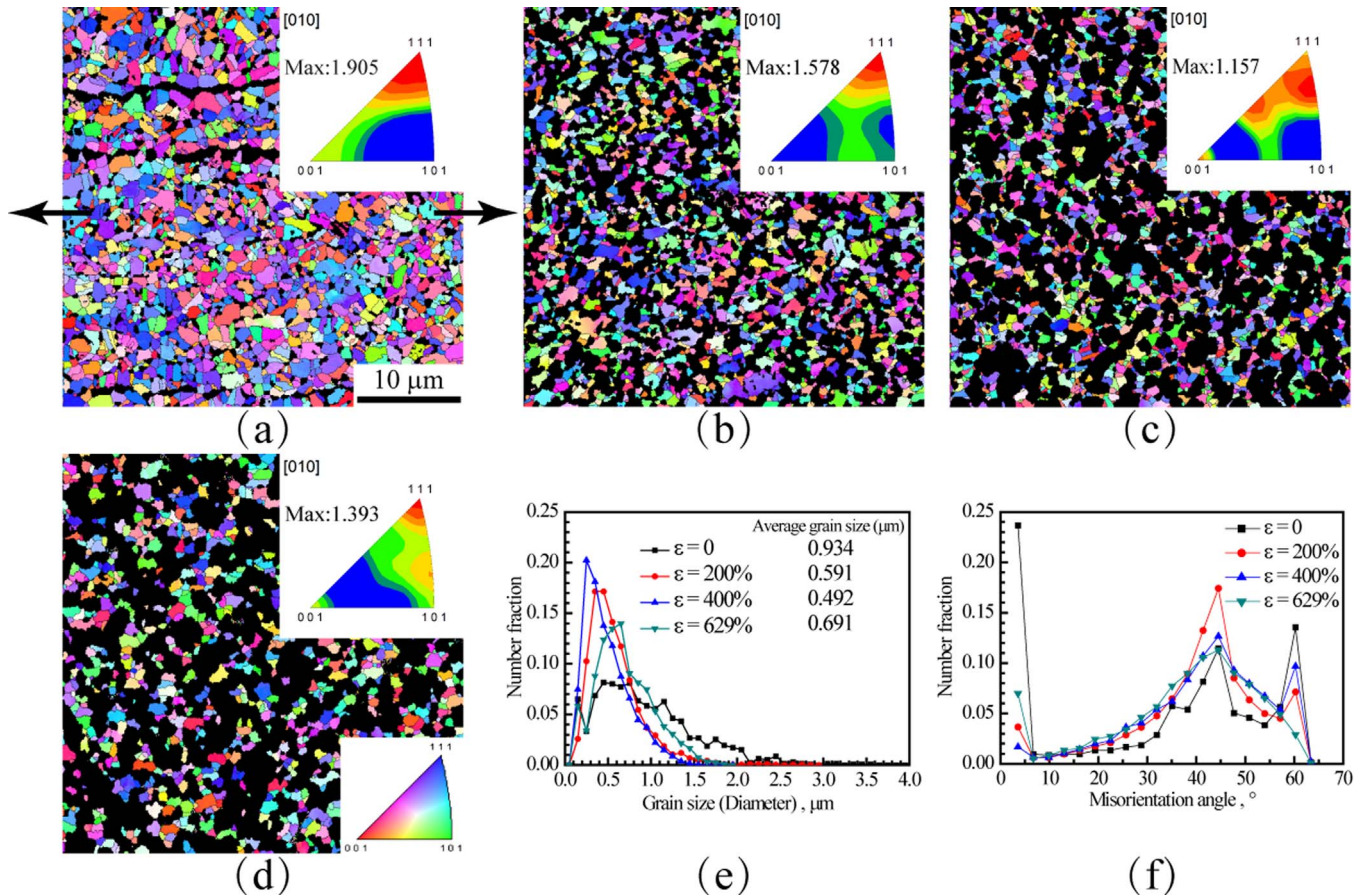
Fig. 7. The EBSD IPF images under high temperature tensile deformation (under temperature of 973 K and strain rate of 10^{-3}/s) for B2 phase: (a) $\varepsilon = 0$; (b) $\varepsilon = 200\%$; (c) $\varepsilon = 400\%$; (d) $\varepsilon = 629\%$. (e) The corresponding grain size distributions at varying tensile strains. (f) The corresponding misorientation angle distributions at varying tensile strains.
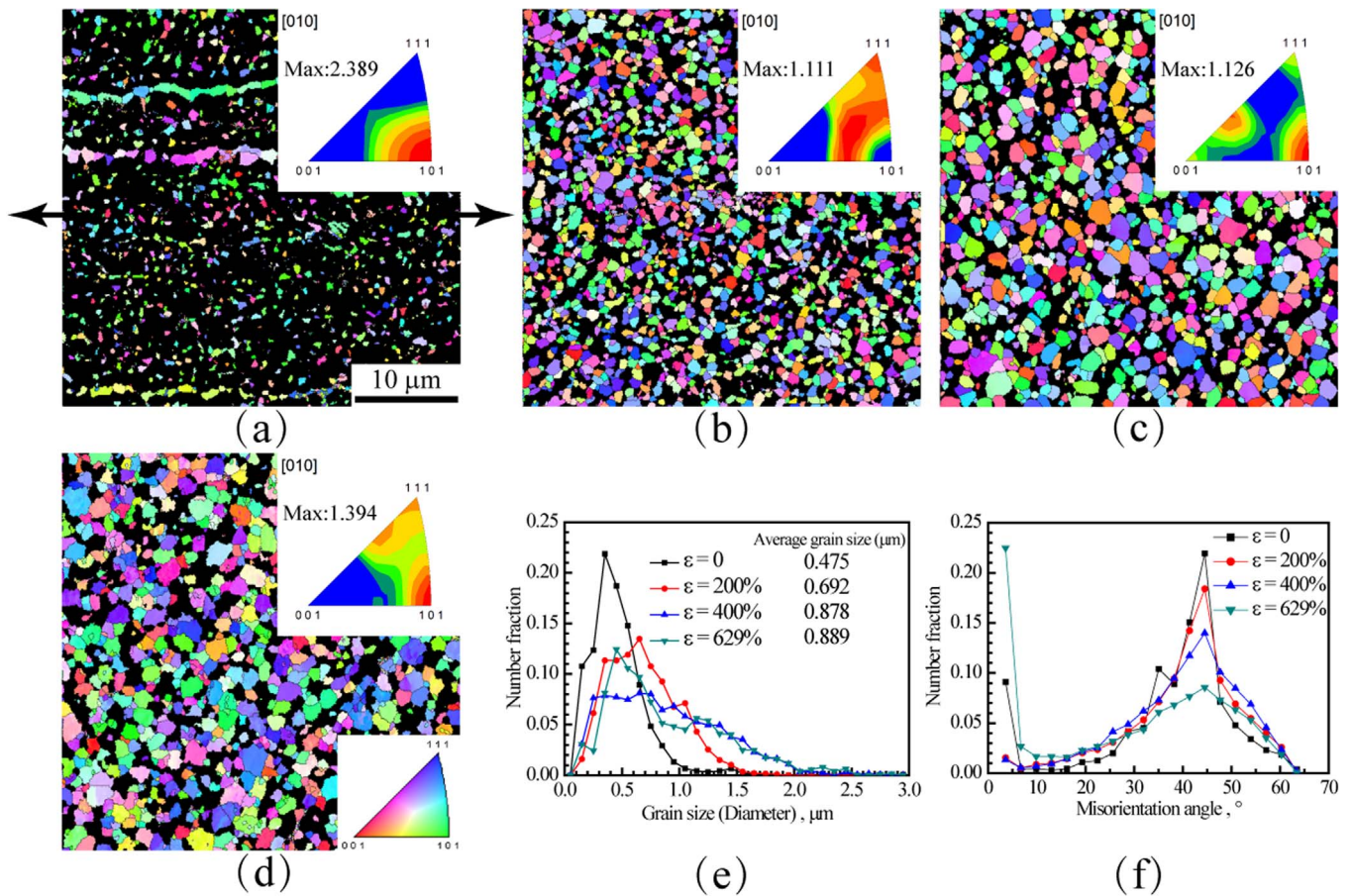
where $V'_{B_2} = V_{B_2}/V_{B_2,\text{saturation}}$ ($V_{B_2,\text{saturation}}$ is the volume fraction of transformed B2 phase after complete transformation) is the normalized volume fraction of transformed B2 phase, t is the time and k is a constant.

The normalized volume fraction of transformed B2 phase as a function of time for both static annealing and high temperature tensile deformation are plotted in Fig. 5(c). Then the $\ln \ln(\frac{1}{1-V'_{B_2}})$ vs. $\ln t$ curves for both conditions are shown in Fig. 5(d). The transformation characteristic exponent n for both conditions can be extracted from Fig. 5(c) as the slopes of the two curves. The obtained n is 1.54 for static annealing while is 1.26 for high temperature tensile deformation. These values are relatively small, suggesting that the transformation is indeed diffusion controlled for the B2 phase growth along GBs or triple junctions [31,35]. These values also suggest that the diffusion controlled growth is all shapes growing from small dimensions for static annealing (n value is about 1.5), while the diffusion controlled growth is growth of particles with appreciable initial volume for high temperature tensile deformation (n value is between 1 and 1.5) [35]. These suggestions are also consistent with the EBSD observations in Fig. 4. Based on the above discussions, the B2 phase growth is shown to be diffusion controlled along defects (subboundaries, GBs). Thus, the strain-enhanced transformation mentioned earlier should be due to the kinetic effect, since the defect concentrations (dislocation wall, subboundary, etc.) would increase with increasing strain in the superplastically loaded specimens, resulting in higher diffusion-controlled phase transformation.

The evolutions of grain morphology, misorientation and size (Inverse Pole Figure, IPF) under high temperature tensile deformation (under temperature of 973 K and strain rate of 10^{-3}/s) for both fcc austenite phase and B2 phase are displayed in Fig. 6 and Fig. 7, respectively. B2 phase in Fig. 6 and fcc austenite phase in Fig. 7 are blacked out for clarity. In each figure, texture is also provided as an inset and the tensile direction is also indicated by arrows. At the first stage (from undeformed state to 400% strain), it is can be clearly seen that the maximum texture intensity decreases from 1.905 to 1.157 for fcc austenite phase, and decreases from 2.389 to 1.126 for B2 phase. High temperature deformation at the first stage results in the weakening and randomization of the initial textures. It is well known that the weakening of texture and intensity during deformation are closely related to GBS and grain rotation [36–39]. As indicated in Fig. 7, ⟨101⟩ texture is much weakened for B2 phase when the tensile strain is from 0% to 200%, which could also be attributed to the texture weakening by transformation besides by GBS and grain rotation. The GBS might also be partly accommodated by the deformation-enhanced phase transformation from fcc austenite phase to B2 phase, similar to the idea in the previous research [31]. The misorientation angle distributions at varying tensile strains for fcc austenite phase and B2 phase are shown in Fig. 6(f) and Fig. 7(f), respectively. It is observed that the fraction of very low angle grain boundaries (LAGBs) with misorientation angle < 5° decreases at the first stage for both phases. These changes indicate that the very LAGBs have been transited and migrated into high angle grain boundaries (HAGBs with misorientation angle > 15°), and this transition could be attributed to dynamic recrystallization (DRX) by generation of numerous new grains with HAGBs [37].

The grain size distributions at varying tensile strains for fcc austenite phase and B2 phase are shown in Fig. 6(e) and Fig. 7(e), respectively. It is clearly observed that the grain size of fcc austenite phase monotonically decreases while the grain size of B2 phase monotonically increases at the first stage. The grain size reduction for fcc austenite phase can be attributed to the DRX and the phase transformation inside the fcc austenite grains. While the grain growth for B2 phase can be attributed to the nucleation and the propagation of phase
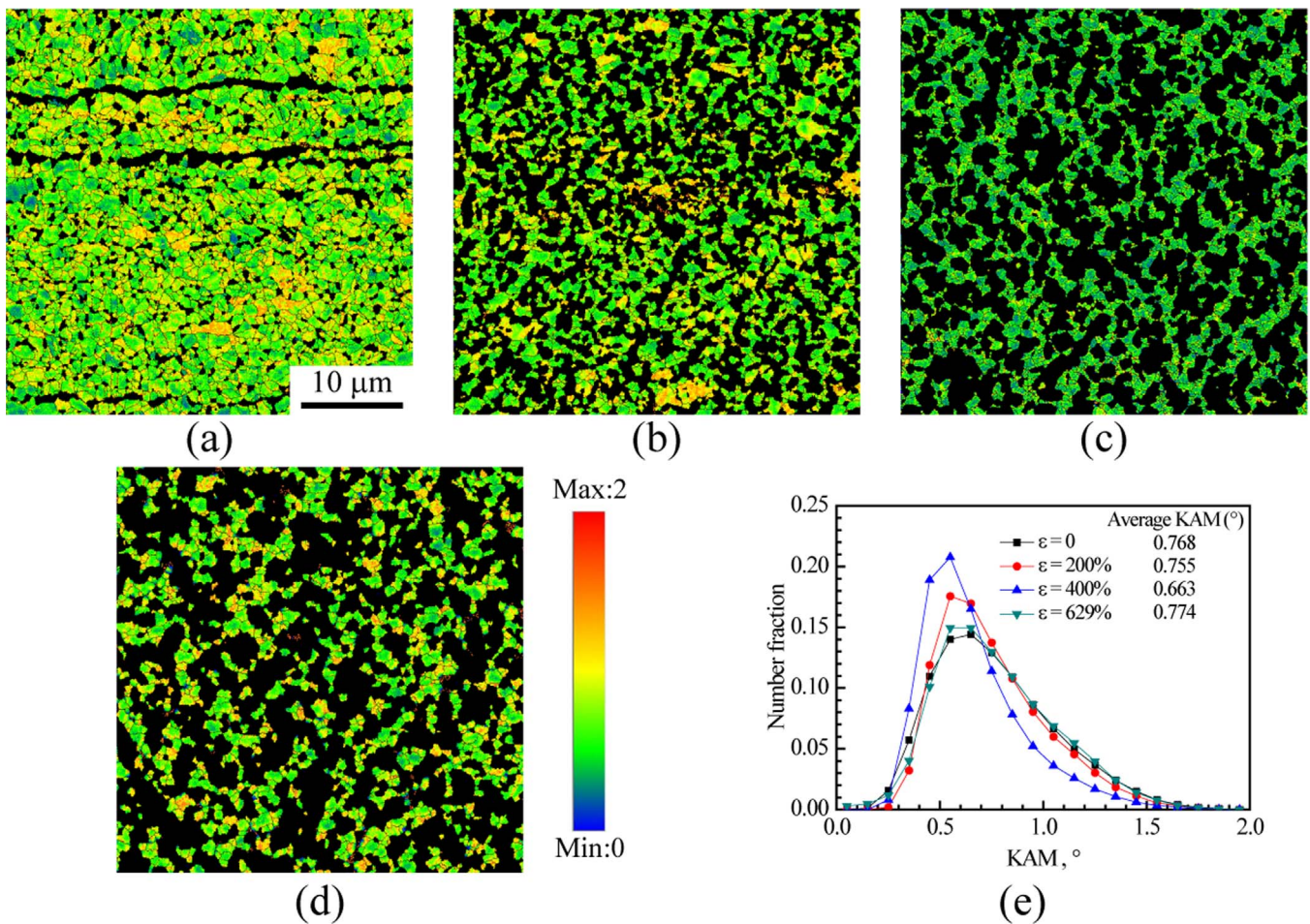
Fig. 8. The KAM images under high temperature tensile deformation (under temperature of 973 K and strain rate of 10^{-3}/s) for fcc austenite phase: (a) $\varepsilon = 0$; (b) $\varepsilon = 200\%$; (c) $\varepsilon = 400\%$; (d) $\varepsilon = 629\%$. (e) The corresponding KAM distributions at varying tensile strains.

transformation process. Although slight grain refinement/growth is observed for both phases, the grain sizes of both phases are observed to always remain sub-micron level during the high temperature deformation. As indicated in previous research [1], UFG metals processed by SPD usually can achieve better superplastic behavior than conventional CG metals. Thus, this relatively stable UFG grains in both phase also help to achieve excellent superplasticity in this HSSS.

B2 phase is harder than fcc austenite phase, thus the benefits of the phase transformation in this HSSS are apparent to accommodate the plastic strain under high temperature. This effect is similar to the effect of transformation induced plasticity (TRIP) for austenite steels [40,41], where stress induced martensite can accommodate the local strain concentration as a medium. The only difference between TRIP steels and the HSSS is the transformation is diffusion controlled for the present case. The strain-enhanced transformation can provide two advantages contributing to large elongation during the high temperature deformation: Firstly, the transformation strain itself can prevent early void formation by accommodating the large stress during GBS; Secondly, the B2 phase can strengthen the strain concentration region and thus help to maintain large homogeneous deformation by preventing early necking formation [41]. Thus, as a summary, the superplastic behaviors at the first stage can be attributed to the diffusional transformation from fcc austenite phase to B2 phase coupled with GBS.

While at the second stage (from 400% to 629%), it is observed that the maximum texture intensity slightly rises again from 1.157 to 1.393 for fcc austenite phase, and increases from 1.126 to 1.394 for B2 phase. It is also observed that the fraction of very LAGBs with misorientation angle < 5° rises again at the second stage for both phases. In order to

illustrate the deformation mechanisms for the second stage, the KAM images at varying tensile strains for fcc austenite phase and B2 phase are shown in Fig. 8 and Fig. 9, respectively. The magnitude of KAM generally represents the dislocation density (especially for geometrically necessary dislocations, GNDs) in the grain interior. Then, the KAM distributions at varying tensile strains for both phases are summarized in Fig. 8(e) and Fig. 9(e). It is observed that the average KAM decreases from 0.768 to 0.663 for fcc austenite phase and reduces from 0.786 to 0.513 for B2 phase at the first stage, which is consistent with the reduction of the fraction of very LAGBs and DRX as mentioned earlier. While the average KAM rises again for both phases at the second stage, which will result in an increase of the fraction of very LAGBs as shown in Fig. 6(f) and Fig. 7(f). This increase for KAM also indicates the increase of dislocation density, thus indicates the significant dislocation activities in the grain interior at the second stage.

It is indicated from previous research [15] that the superplastic behaviors for metals and alloys at a given temperature and varying strain rates can be categorized into three well defined regions having different values for the SRS (m): In region I at low strain rates, SRS is generally low (~ 0.2) and the behavior is controlled by impurity effects; In region II over a range of intermediate strain rates, SRS is generally high (~ 0.5) and the flow behavior can be attributed to GBS; In region III at high strain rates, SRS is low again (~ 0.2) and the metals and alloys deform by the glide and climb of dislocations within the grains (dislocation creep). In Fig. 3(a), it is observed that the SRS is about 0.47 at the strain rate range of 10^{-4} to 10^{-3}/s, is about 0.34 at the strain rate range of 10^{-3} to 10^{-2}/s, and is about 0.20 at the strain rate range of 10^{-2} to 10^{-1}/s at a given temperature of 973 K. Thus, regions II and
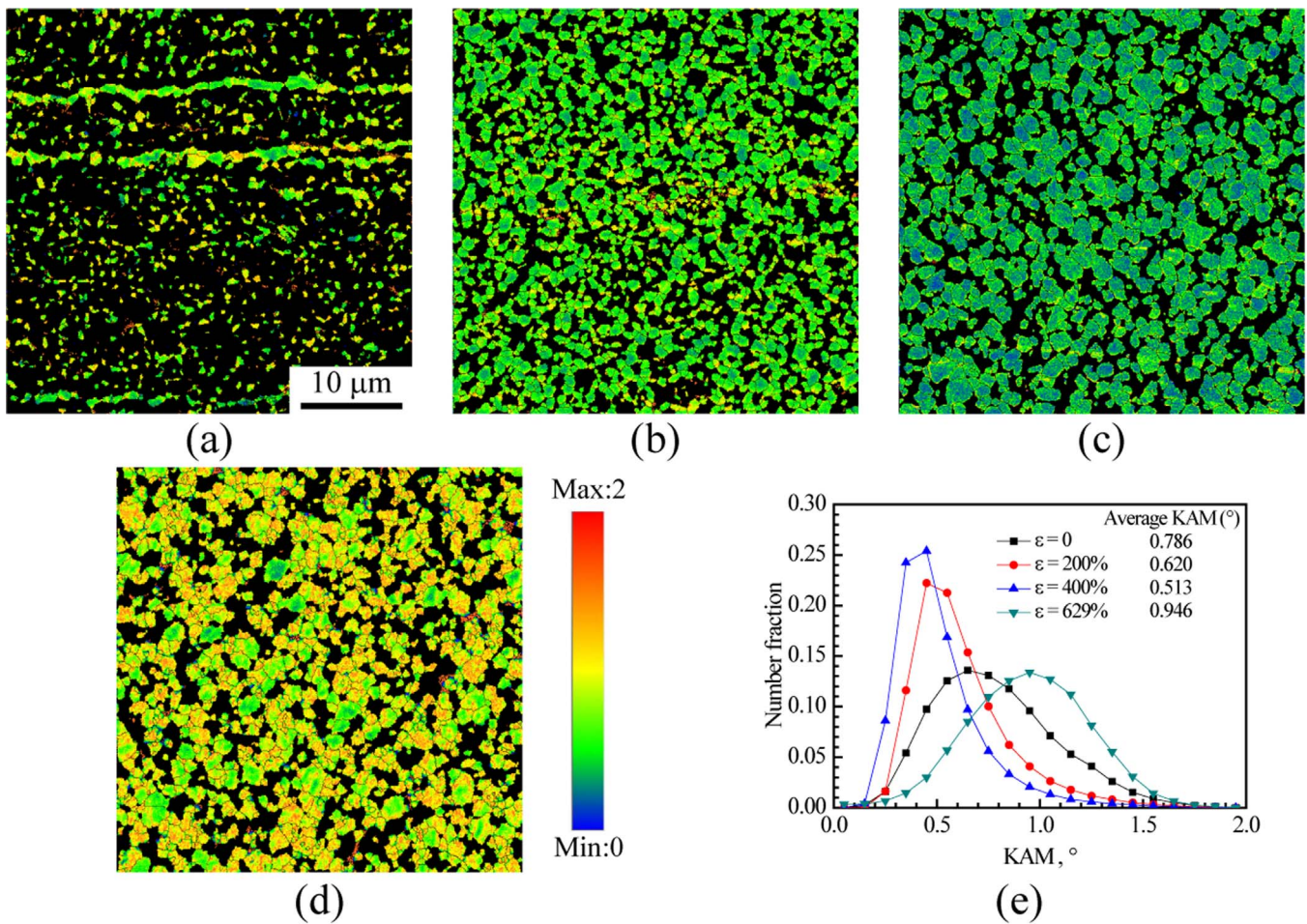
Fig. 9. The KAM images under high temperature tensile deformation (under temperature of 973 K and strain rate of 10^{-3}/s) for B2 phase: (a) $\varepsilon = 0$; (b) $\varepsilon = 200\%$; (c) $\varepsilon = 400\%$; (d) $\varepsilon = 629\%$. (e) The corresponding KAM distributions at varying tensile strains.
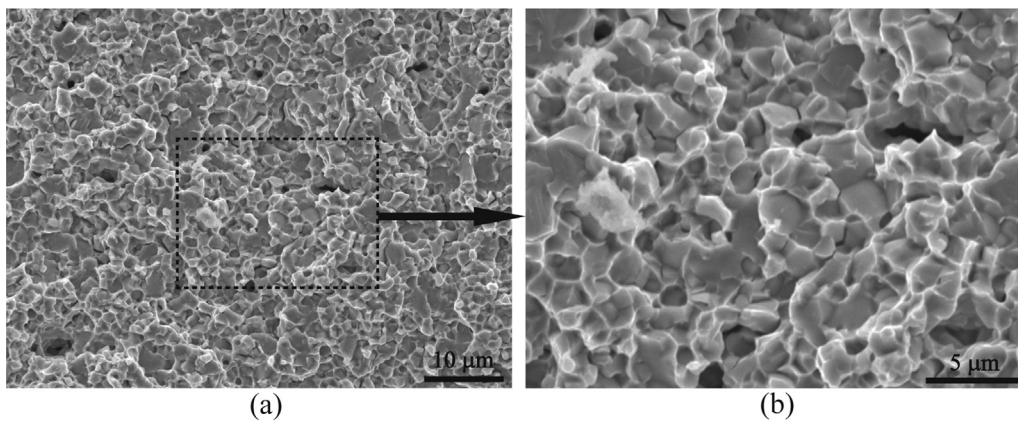

Fig. 10. (a) The SEM images of final fracture surface for the high temperature deformation under temperature of 973 K and strain rate of 10^{-3}/s; (b) The corresponding close-up view for the rectangular area in (a).

III are observed in strain rate range of the present experiments, region I should be in the even lower strain rate range. As indicated from the inset of Fig. 2(c), the final fracture shape indicates a diffusive necking at the center part of the gauge section, thus the realistic strain rate at the center part of the gauge section at the second stage should be much higher than the initial strain rate. Thus, the observed increase for KAM and the resultant intragranular slips at the second stage should be attributed to this increase in the realistic strain rate by diffusive necking (this suddenly increase in strain rate can turn the initial region II into the current region III).

The SEM images of final fracture surface for the high temperature deformation under temperature of 973 K and strain rate of 10^{-3}/s are shown in Fig. 10. The fracture is observed to be ductile with dimples. These dimples appear to be formed by pulling out the B2 particle from the fcc austenite matrix or fracturing the B2 particle during the high temperature deformation. Thus, the higher density of the interfaces, the more energy needed to be consumed for the final fracture. Thus, the fraction of interfaces should be considered as a controlling factor for the superplasticity. As a result, the superplasticity of this HSSS could be further enhanced by increasing the density of interface, i.e., refining the sizes of both phases. Refining grain sizes can promote GBS for better superplasticity by an increase of GB density on one hand, and can raise the resistance to final fracture by an increase of phase boundary density on the other hand.

4. Conclusions

In the present study, the superplastic behaviors of a HSSS with dual-phase microstructure and ultrafine grains have been investigated. The main findings are summarized as follows:

(1) The UFG HSSS exhibits excellent superplastic properties. The microstructure observations at interrupted strains for tests under temperature of 973 K and at strain rate of 10^{-3}/s have provided evidences of different mechanisms for two stages.
(2) At the first stage (strain range from 0% to 400%), the superplastic flow can be attributed to the strain-enhanced diffusional transformation from fcc austenite phase to B2 phase coupled with GBS. The average size of the B2 precipitates as a function of time follows the well-known $t^{1/2}$ diffusion rule, the activation energy is about 216 kJ/mol and the transformation characteristic exponent n is close to 1.26 under high temperature tensile deformation, suggesting that the transformation is indeed diffusion controlled along defects. The grain sizes of both phases are observed to be relatively stable and remain always sub-micron level during the superplastic deformation, facilitating the superplastic flow.
(3) At the second stage (strain range from 400% to 629%), the diffusive necking results in an increase in the realistic strain rate and a transition from region II to region III, thus the glide and climb of dislocations in the grain interior should be the dominant mechanism for this stage. The current results should provide insights for better understanding of the superplastic behaviors and for the part forming of this HSSS in automobile industry.

Acknowledgements

References

[1] S.X. McFadden, R.S. Mishra, R.Z. Valiev, A.P. Zhilyaev, A.K. Mukherjee, Low-temperature superplasticity in nanostructured nickel and metal alloys, Nature 398 (1999) 684–686.

[2] G. Rai, N.J. Grant, On the measurements of superplasticity in an Al-Cu Alloy, Metall. Trans. A 6A (1975) 385–390.

[3] M. Mabuchi, K. Ameyama, H. Iwasaki, K. Higashi, Low temperature superplasticity of AZ91 magnesium alloy with non-equilibrium grain boundaries, Acta Mater. 7 (1999) 2047–2057.

[4] G. Frommeyer, J.A. Jiménez, Structural superplasticity at higher strain rates of hypereutectoid Fe-5.5Al-1Sn-1Cr-1.3C steel, Metall. Mater. Trans. A 36A (2005) 295–300.

[5] H. Zhang, B. Bai, D. Raabe, Superplastic martensitic Mn-Si-Cr-C steel with 900% elongation, Acta Mater. 59 (2011) 5787–5802.

[6] G. Frommeyer, W. Kowalski, R. Rablbauer, Structural superplasticity in a fine-grained eutectic intermetallic NiAl-Cr alloy, Metall. Mater. Trans. A 37A (2006) 3511–3517.

[7] L. Lu, M.L. Sui, K. Lu, Superplastic extensibility of nanocrystalline copper at room temperature, Science 287 (2000) 1463–1466.

[8] T.G. Langdon, The mechanical properties of superplastic materials, Metall. Trans. A 13A (1982) 689–701.

[9] E.M. Taleff, M. Nagao, K. Higashi, O.D. Sherby, High-strain-rate superplastocoty in ultrahigh-carbon steel containing 10 wt% Al(UHCS-10Al), Scr. Mater. 34 (1996) 1919–1923.

[10] R.M. Imayev, O.A. Kaibyshev, G.A. Salishchev, Mechanical behaviour of fine grained TiAl intermetallic compound-I. Superplasticity, Acta Metall. Mater. 40 (1992) 581–587.

[11] G. Frommeyer, C. Derder, J.A. Jiménez, Superplasticity of Fe₃Al(Cr), Mater. Sci. Technol. 18 (2002) 981–986.

[12] D.L. Lin, A.D. Shan, D.Q. Li, M.W. Chen, Y. Liu, Superplastic behavior of large grained iron alluminides, Mater. Sci. Forum 243–245 (1997) 619–630.

[13] D.L. Lin, D.Q. Li, Y. Liu, Superplasticity in large-grained FeAl based intermetallic alloys, Intermetallics 6 (1998) 243–256.

[14] J.A. Jiménez, G. Frommeyer, M. Carsí, O.A. Ruano, Superplastic properties of a δ/γ stainless steel, Mater. Sci. Eng. A A307 (2001) 134–142.

[15] M. Kawasaki, T.G. Langdon, Principles of superplasticity in ultrafine-grained materials, J. Mater. Sci. 42 (2007) 1782–1796.

[16] T.G. Langdon, Seventy-five years of superplasticity: historic developments and new opportunities, J. Mater. Sci. 44 (2009) 5998–6010.

[17] G. Frommeyer, U. Bruex, Microstructures and mechanical properties of high-strength Fe-Mn-Al-C light-weight TRIPLEX steels, Steel Res. Int. 77 (2006) 627–633.

[18] J.D. Yoo, S.W. Hwang, K.-T. Park, Factors influencing the tensile behavior of a Fe-28Mn-9Al-0.8C steel, Mater. Sci. Eng. A 508 (2009) 234–240.

[19] S.W. Hwang, J.H. Ji, E.G. Lee, K.-T. Park, Tensile deformation of a duplex Fe-20Mn-9Al-0.6C steel having the reduced specific weight, Mater. Sci. Eng. A 528 (2011) 5196–5203.

[20] I. Gutierrez-Urrutia, D. Raabe, Influence of Al content and precipitation state on the mechanical behavior of austenitic high-Mn low-density steels, Scr. Mater. 68 (2013) 343–347.

[21] D. Raabe, H. Springer, I. Gutierrez-Urrutia, F. Roters, M. Bausch, J.-B. Seol, M. Koyama, P.-P. Choi, K. Tsuzaki, Alloy design, combinatorial synthesis, and microstructure–property relations for low-density Fe-Mn-Al-C austenitic steels, J. Miner. Met. Mater. Soc. 66 (2014) 1845–1856.

[22] R. Rana, C. Lahaye, R.K. Ray, Overview of lightweight ferrous materials strategies and promises, J. Miner. Met. Mater. Soc. 66 (2014) 1734–1746.

[23] S.S. Sohn, H. Song, B.C. Suh, J.H. Kwak, B.J. Lee, N.J. Kim, S. Lee, Novel ultra-high-strength (ferrite + austenite) duplex lightweight steels achieved by fine dislocation substructures (Taylor lattices), grain refinement, and partial recrystallization, Acta Mater. 96 (2015) 301–310.

[24] S.H. Kim, H. Kim, N.J. Kim, Brittle intermetallic compound makes ultrastrong low-density steel with large ductility, Nature 518 (2015) 77–79.

[25] M.X. Yang, F.P. Yuan, Q.G. Xie, Y.D. Wang, E. Ma, X.L. Wu, Strain hardening in Fe-16Mn-10Al-0.86 C-5Ni high specific strength steel, Acta Mater. 109 (2016) 213–222.

[26] W. Wang, H.S. Zhang, M.X. Yang, P. Jiang, F.P. Yuan, X.L. Wu, Shock and spall behaviors of a high specific strength steel: effects of impact stress and microstructure, J. Appl. Phys. 121 (2017) 135901.

[27] O.D. Sherby, Advances in superplasticity and in superplastic materials, ISIJ Int. 29 (1989) 698–716.

[28] W.J. Kim, K. Higashi, J.K. Kim, High strain rate superplastic behaviour of powder-metallurgy processed 7475Al+0.7Zr alloy, Mater. Sci. Eng. A 260 (1999) 170–177.

[29] Z.Y. Ma, R.S. Mishra, M.W. Mahoney, Superplastic deformation behaviour of friction stir processed 7075Al alloy, Acta Mater. 50 (2002) 4419–4430.

[30] M. Calcagnotto, D. Ponge, E. Demir, D. Raabe, Orientation gradients and geometrically necessary dislocations in ultrafine grained dual-phase steels studied by 2D and 3D EBSD, Mater. Sci. Eng. A 527 (2010) 2738–2746.

[31] K.L. Yang, J.C. Huang, Y.N. Wang, Phase transformation in the β phase of super α₂ Ti₃Al base alloys during static annealing and superplastic deformation at 700-100°C, Acta Mater. 51 (2003) 2577–2594.

[32] C.G. McKamey, P.J. Maziasz, J.W. Jones, Effect of addition of molybdenum or niobium on creep-rupture properties of Fe₃Al, J. Mater. Res. 7 (1992) 2089–2106.

[33] J.D. Whittenberger, The influence of grain size and composition on slow plastic flow in FeAl between 1100 and 1400 K, Mater. Sci. Eng. 77 (1986) 103–113.

[34] D. Lin, T.L. Lin, A. Shan, M. Chen, Superplasticity in large-grained Fe₃Al alloys, Intermetallics 4 (1996) 489–496.

[35] J.W. Christian, The Theory Of Transformations In Metals And Alloys, Pergamon Press, Oxford, NY, 1975, pp. 538–546.

[36] Y. Huang, Evolution of microstructure and texture during hot deformation of a commercially processed supral100, J. Mater. Sci. Technol. 28 (2012) 531–536.

[37] Z.G. Liu, P.J. Li, L.T. Xiong, T.Y. Liu, L.J. He, High-temperature tensile deformation behavior and microstructure evolution of Ti55 titanium alloy, Mater. Sci. Eng. A 680 (2017) 259–269.

[38] H. Watanabe, K. Kurimoto, T. Uesugi, Y. Takigawa, K. Higashi, Isotropic superplastic flow in textured magnesium alloy, Mater. Sci. Eng. A 558 (2012) 656–662.

[39] L. Cheng, J.S. Li, X.Y. Xue, B. Tang, H.C. Kou, E. Bouzy, Superplastic deformation mechanisms of high Nb containing TiAl alloy with (α₂+γ) microstructure, Intermetallics 75 (2016) 62–71.

[40] O. Grässel, L. Krüger, G. Frommeyer, L.W. Meter, High strength Fe-Mn-(Al, Si) TRIP/TWIP steels development-properties-application, Int. J. Plast. 16 (2000) 1391–1409.

[41] X. Ren, M. Hagiwara, Displacive precursor phenomena in Ti-22Al-27Nb intermetallic compound prior to diffusional transformation, Acta Mater. 49 (2001) 3971–3980.